sustainable chemistry

MDPI

Article

Selective Biosorption of Hg(II), Cd(II), and Pd(II) on Functionalized Chitosan (–SH/–COO$^-$): A DFT Study with ESP/MEP and NCI/RGD Analyses

Joaquín Hernández-Fernández [1,2,*], Rafael González-Cuello [3] and Rodrigo Ortega-Toro [3]

[1] Chemistry Program, Department of Natural and Exact Sciences, University of Cartagena, San Pablo Campus, Cartagena de Indias 130015, Colombia
[2] Department of Natural and Exact Sciences, Universidad de la Costa, Barranquilla 080002, Colombia
[3] Food Packaging and Shelf-Life Research Group (FP&SL), Food Engineering Program, University of Cartagena, Cartagena de Indias 130015, Colombia; rortegap1@unicartagena.edu.co (R.O.-T.)
* Correspondence: jhernandezf@unicartagena.edu.co

Abstract

In this work, density functional theory (DFT) was used to comparatively investigate the thermodynamic and electronic factors governing the association of Cd(II), Hg(II), and Pd(II) with native chitosan (CTS) and functionalized derivatives (CTS–COOH, CTS–COO−, CTS–NH_3^+, and CTS–SH). Representative acid–base states were considered to approximate changes in site availability, and a uniform explicit microhydration scheme was adopted to enable controlled relative comparisons across metals and materials. Within this framework, the calculated free energies suggest metal-dependent affinity regimes: the carboxylic microenvironment favors Cd(II), the thiolated microenvironment provides the most favorable association for Hg(II), and native CTS affords the strongest calculated stabilization for Pd(II). Geometry optimizations show that most complexes retain the first hydration sphere of the metal, indicating that stabilization is dominated by outer-sphere association rather than by systematic first-sphere ligand substitution. ESP/MEP maps reveal that the heterogeneity and directionality of the electrostatic landscape govern selectivity. In contrast, NCI analysis supports a cooperative contribution of weak interactions and second-sphere organization. These results provide a comparative electronic framework to guide future experimental validation of selective metal capture by functionalized chitosan materials.

Keywords: chemical functionalization; acid–base speciation; explicit microhydration; metal–ligand complexation; thermodynamic affinity; induced polarization

Check for updates

Academic Editor: Matthew Jones

Received: 19 February 2026
Revised: 26 March 2026
Accepted: 2 April 2026
Published: 6 April 2026

Copyright: © 2026 by the authors. Licensee MDPI, Basel, Switzerland. This article is an open access article distributed under the terms and conditions of the Creative Commons Attribution (CC BY) license.

1. Introduction

Heavy-metal contamination in aqueous matrices remains a priority issue due to its persistence, bioaccumulation, and systemic toxicity, with impacts ranging from neurotoxic and renal alterations to chronic risks even at low concentrations [1]. In particular, Hg(II), Cd(II), and Pd(II) are among the cations of greatest concern due to their environmental mobility and the regulatory pressure on drinking water and effluents [2,3]. In this context, the development of low-cost adsorbents with high efficiency and genuine selectivity under ionic competition remains a scientific and technological bottleneck, because removal does not depend solely on 'capacity' but on the fine chemistry of the active site and the acid–base microenvironment that governs metal and polymer speciation [1–3].

Chitosan, a partially deacetylated derivative of chitin, is an especially attractive platform for biosorption due to its abundance, biodegradability, and high density of amino and hydroxyl groups that can coordinate metal cations [4,5]. From a physicochemical standpoint, its performance is governed by structural variables (degree of deacetylation, acetyl distribution, molar mass), conformational factors (flexibility and accessibility of sites), and medium effects (pH, ionic strength, site competition), which explains why 'similar' adsorbents may display different selectivities toward Hg(II), Cd(II), and Pd(II). Therefore, targeted chemical modification of chitosan should not be viewed as an empirical adjustment, but rather as a strategy to reconfigure the hardness/softness of the coordinating site, its effective charge, and its ability to stabilize complexes through primary (coordination) and secondary interactions (H-bonding, electrostatic contacts) [4–6].

Functionalization with thiol (–SH/–S^-) and carboxylate (–CH_2–COO^-) groups is particularly relevant because it enables 'programming' of coordination preferences: Hg(II), as a soft acid, tends to be stabilized by soft bases (thiolates), whereas Cd(II) and Pd(II) often exhibit borderline behavior in which covalent and electrostatic contributions coexist; by contrast, carboxylates provide harder sites and an anionic architecture that favors capture via Coulombic attraction and multidentate chelation under conditions where deprotonation is significant [7–10]. Moreover, the introduction of carboxylic motifs (e.g., N-/O-carboxymethylation) modifies complexation thermodynamics and the enthalpy–entropy balance of metal–polymer associating, while hybrid chitosan–CMC networks offer 'green' routes to stabilize multiple sites and enhance performance in Pd(II)/Cd(II) removal [8,9].

Nevertheless, in many biosorption systems, the mechanistic discussion remains incomplete: removal is reported, but it is not resolved which interaction dominates (N/O/S coordination, ion pairing, charge transfer), how it changes with adsorbent protonation, or why selectivity emerges among competing cations. In this scenario, computational chemistry provides a traceable framework to connect structure and affinity: previous DFT studies on chitosan and its derivatives have shown that the nature of the coordinating heteroatom, local geometry, and electronic redistribution explain stability trends for Hg(II) and Pd(II) [11–13], and even model metal–glucosamine-unit systems have been useful to decompose bonding contributions and site preferences. To approximate realistic aqueous conditions, continuum solvation models (e.g., SMD) are critical for estimating relative energies and electronic profiles that are comparable across complexes [14]. In parallel, NBO analysis enables quantification of donor/acceptor (donor→acceptor) interactions and rationalization of charge transfer [15]. Complementary electron-density analyses can further clarify whether stabilization arises from localized coordinative contacts or from broader weak-interaction networks. In this context, electrostatic potential mapping reveals the spatial distribution of attractive and repulsive regions. In contrast, NCI analysis visualizes dispersive, attractive, and steric contributions that help organize the metal–biopolymer assembly [16–18]. Tools such as Multiwfn facilitate reproducible extraction of ESP and NCI descriptors from DFT wavefunctions [18], and platforms such as Gaussian enable a standard implementation of these workflows [19].

2. Materials and Methods

2.1. Study Design and System Matrix

The selective biosorption of Hg(II), Cd(II), and Pd(II) on native chitosan and chitosan functionalized with thiol (–SH) and carboxymethyl (–CH_2–COOH/–CH_2–COO^-) groups was evaluated under a comparative framework designed to isolate the effects of donor-site identity (N/O/S), the metal ion, and the acid–base state (as a pH proxy) [20–22].

Selectivity was quantified using free-energy differences (ΔGassoc) and rationalized using electron-density–based analyses (ESP/MEP and NCI/RDG) [23,24].

2.2. Chitosan Model Construction and Functionalization

Chitosan was represented as a finite oligomer (tetramer) with capped termini to minimize edge artifacts [25]. Functional groups were introduced on an internal repeating unit to preserve a representative local environment. Native chitosan was modeled with available $–NH_2$ (C2) and –OH (C3/C6) sites [26,27]. Thiolated chitosan was represented via N-functionalization at C2 using a short substituent bearing an accessible sulfur donor ($–NH–CH_2–CH_2–SH$) to capture the soft character of the site [28]. Carboxymethylated chitosan was modeled preferentially as O-carboxymethylation at C6 ($–O–CH_2–COOH$) and its deprotonated active form ($–O–CH_2–COO^-$), since this motif introduces an anionic site capable of O-chelation and enhances electrostatic interactions in aqueous media [27,29].

2.3. Protonation States and Charge Consistency

To approximate the effect of pH on the availability of coordinating sites, representative acid–base states were considered for each material: $–NH_2$ versus $–NH_3^+$ and –COOH versus –COO−. These states were not intended to reproduce the full distribution of solution species at a given experimental pH, but rather to probe how local protonation modifies donor availability, electrostatic organization, and relative metal affinity within a controlled comparative framework [30,31]. In systems containing oppositely charged groups, chemically reasonable zwitterionic arrangements were considered when appropriate, while preserving total-charge consistency across the series being compared. This strategy was adopted to ensure that differences in calculated association free energies could be interpreted primarily in terms of local chemical environment rather than arbitrary charge imbalance [32].

2.4. Metal Species, Microhydration, and Initial Complexes

Cd^{2+}, Hg^{2+}, and Pd^{2+} were represented as explicitly microhydrated cationic complexes, $[M(H_2O)_5]^{2+}$, to provide a uniform reference state for comparative calculations across metals and adsorbents. This choice was not intended to reproduce the full aqueous speciation or preferred coordination number of each metal in solution, which may differ among Cd(II), Hg(II), and Pd(II), but rather to establish a controlled microhydrated framework in which hydration–adsorption competition could be evaluated consistently. For each material–metal–acid–base combination, initial complexes were constructed by placing the hydrated metal near the most relevant donor region (N-, O-, or S-containing environments), while allowing full structural relaxation during geometry optimization. In this way, the final optimized structures determine whether the system evolves toward outer-sphere association, incipient inner-sphere contact, or retention of the primary hydration shell.

2.5. DFT Calculations, Microhydration, and Thermodynamics (Gaussian)

Geometry optimizations and vibrational analyses were carried out with Gaussian 16 using two density functionals, M06-2X-D3 and ωB97X-D, in combination with the LANL2DZ basis set and its associated effective core potentials for the heavy elements [33–37]. This dual-functional strategy was adopted to examine the internal robustness of the calculated trends rather than to establish a formal benchmark based solely on frontier-orbital energies. For Hg and Pd, scalar-relativistic effects are only partially incorporated via the effective core potential embedded in LANL2DZ, and this limitation should be considered when interpreting absolute energy values.

To approximate hydration effects, an explicit microhydration scheme was employed in which each metal was introduced as $[M(H_2O)_5]^{2+}$ [38,39]. Geometry optimization and

frequency analysis were performed at the same level of theory, and only structures with no imaginary frequencies were accepted as true minima. Because the optimized minima retained the five-water first coordination sphere in the systems discussed here (k = 0), the association free energy was evaluated as:

$$\Delta G_{assoc} = G([Biopol\cdots M(H_2O)_5]^{2+}) - G(Biopol) - G([M(H_2O)_5]^{2+}) \quad (1)$$

where Biopol denotes the adsorbent model, within this framework, more negative ΔGassoc values indicate a more favorable formation of the microhydrated metal–adsorbent adduct. These values are interpreted comparatively across metals and functional groups under a uniform reference scheme [40].

2.6. Electronic/Topological Post-Processing (Multiwfn) and Comparison Criteria

Wavefunctions were exported to .fchk files and analyzed in Multiwfn to link selectivity with electronic descriptors. Electrostatic potential maps (ESP/MEP) were computed to identify attractor regions induced by –SH and $–COO^-$, and NCI/RDG analysis was used to visualize the contribution of noncovalent interactions (H-bonding, dispersive contacts, and steric repulsion) that stabilize or penalize the complexes. System-to-system comparisons were performed while keeping the solvation scheme, microhydration size within each series, level of theory, and thermodynamic criterion (ΔGassoc) constant, and additionally reporting metal–donor distances and final coordination modes as structural support for the analysis [41–43].

3. Results and Discussion

3.1. Geometry Optimization and Selection of the Level of Theory (M06-2X-D3 vs. ωB97X-D; LANL2DZ)

Before constructing the metal–biopolymer complexes and quantifying affinities, an internal benchmark was performed to select the production-level methodology. The adsorbent models (CTS, CTS–COO^-, CTS–COOH, CTS–SH, and CTS–NH_3^+) and the aqueous metal species represented as pentahydrated complexes $[M(H_2O)_5]^{2+}$ (M = Cd, Pd, Hg) were optimized. The comparison was carried out using two density functionals (M06-2X-D3 and ωB97X-D) while keeping the LANL2DZ basis set fixed. No continuum solvation was employed; instead, the aqueous character was incorporated via explicit cation microhydration (Tables 1–4).

Table 1. Energies (Hartree) of the optimized adsorbent models (LANL2DZ).

System	E.syst (M06-2X-D3)	H (M06-2X-D3)	G (M06-2X-D3)	E.syst (ωB97X-D)	H (ωB97X-D)	G (ωB97X-D)
CTS	−1847.592219	−1847.591275	−1847.690401	−1847.711374	−1847.710430	−1847.810395
CTS–COO	−2074.629229	−2074.628285	−2074.737390	−2074.752864	−2074.751920	−2074.862266
CTS–COOH	−2075.294872	−2075.293927	−2075.404614	−2075.420371	−2075.419427	−2075.530119
CTS–SH	−2010.190079	−2010.189135	−2010.298989	−2010.381948	−2010.381004	−2010.485605
CTS–NH_3	−1848.090882	−1848.089938	−1848.193951	−1848.211664	−1848.210719	−1848.324529

Table 2. Frontier orbitals (Hartree) and HOMO–LUMO gap (eV) of the adsorbents (LANL2DZ).

System	HOMO (M06-2X-D3)	LUMO (M06-2X-D3)	ΔEgap (eV)	HOMO (ωB97X-D)	LUMO (ωB97X-D)	ΔEgap (eV)
CTS	−0.26699	0.07333	9.26	−0.28925	0.11376	10.97
CTS–COO	−0.27041	−0.02360	6.72	−0.28669	−0.00570	7.65
CTS–COOH	−0.26686	−0.00424	7.15	−0.28372	0.02549	8.41
CTS–SH	−0.25809	0.01699	7.49	−0.30453	0.05483	9.78
CTS–NH_3	−0.28563	0.07445	9.80	−0.25404	0.09101	9.39

Table 3. Energies (Hartree) of pentahydrate complexes $[M(H_2O)_5]^{2+}$ (LANL2DZ).

Metal	E.syst (M06-2X-D3)	H (M06-2X-D3)	G (M06-2X-D3)	E.syst (ωB97X-D)	H (ωB97X-D)	G (ωB97X-D)
Cd	−429.706827	−429.705883	−429.742192	−429.800060	−429.799116	−429.835733
Pd	−508.249019	−508.248075	−508.283172	−508.401086	−508.400142	−508.435290
Hg	−423.545044	−423.544100	−423.581176	−423.657884	−423.656940	−423.693976

Table 4. Frontier orbitals (Hartree) and HOMO–LUMO gap (eV) of $[M(H_2O)_5]^{2+}$ (LANL2DZ).

Metal	HOMO (M06-2X-D3)	LUMO (M06-2X-D3)	ΔEgap (eV)	HOMO (ωB97X-D)	LUMO (ωB97X-D)	ΔEgap (eV)
Cd	−0.06537	0.01153	2.09	−0.09062	0.05652	4.00
Pd	−0.07752	−0.01086	1.81	−0.09759	0.03513	3.61
Hg	−0.08655	0.02032	2.91	−0.11635	0.05939	4.78

At this stage, absolute electronic energies (E), enthalpies (H), and Gibbs free energies (G), all in Hartree, are reported for traceability purposes only and should not be interpreted as a direct criterion for selecting the production methodology. Likewise, HOMO and LUMO energies, together with the HOMO–LUMO gap, were analyzed descriptively to probe the internal electronic response of the isolated adsorbents and hydrated metal species, rather than as a standalone metric of functional performance. In this context, the comparison between M06-2X-D3 and ωB97X-D was used as an internal consistency test to verify whether the main electronic trends and structural features were preserved across two functionals commonly employed for noncovalent and coordinative systems. The HOMO–LUMO gap was computed as $\Delta Egap = (E_{LUMO} - E_{HOMO}) \times 27.2114$ eV (Table 5).

Table 5. Difference in gap ΔEgap between functionals (ωB97X-D–M06-2X-D3), in eV (Positive values indicate larger HOMO–LUMO gaps with ωB97X-D relative to M06-2X-D3).

System/Metal	(ΔEgap) (eV)
CTS	1.71
CTS–COO	0.93
CTS–COOH	1.27
CTS–SH	2.29
CTS–NH_3	−0.41
$Cd(H_2O)_5^{2+}$	1.91
$Pd(H_2O)_5^{2+}$	1.80
$Hg(H_2O)_5^{2+}$	1.87

Across the adsorbent series, both functionals consistently show that chemical functionalization perturbs the frontier orbital manifold relative to native CTS. The most robust result is the behavior of the carboxylate-containing model, CTS–COO^-, which remains

the most electronically perturbed system in the series, whereas protonated CTS–NH_3^+ is comparatively less activated. This qualitative agreement is more relevant than the absolute magnitude of the gap, because it indicates that both methods preserve the same chemically meaningful ordering of electronic response across the adsorption-site models.

A similar pattern is observed for the pentahydrated metal species, $[M(H_2O)_5]^{2+}$ (M = Cd, Pd, Hg). In these cases, ωB97X-D yields a more conservative electronic description, characterized by larger frontier-orbital separations and a reduced apparent tendency toward excessive charge redistribution. This behavior is methodologically relevant in coordination models where the interaction between hydrated cations and highly polar donor sites must be described without artificially exaggerating charge-transfer contributions. Importantly, however, the role of this comparison is not to identify the "best" functional based on a larger ΔEgap, but to verify that the principal qualitative trends are maintained while avoiding an overdelocalized electronic picture.

Thermal corrections do not materially alter this conclusion. For the adsorbents, the $H - G$ difference remains nearly constant across functionals, and the same behavior is observed for the hydrated metal species. Thus, within this set of isolated structures, the effect of functional choice is governed primarily by electronic effects rather than by thermal contributions.

Because the major qualitative trends are preserved across both methods, and because ωB97X-D provides a balanced treatment of long-range and dispersive effects that is appropriate for metal–adsorbent interactions, ωB97X-D/LANL2DZ was selected as the principal level of theory for the construction and discussion of metal–biopolymer complexes and their associated thermodynamics.

3.2. Ionization Potential and Electron Affinity of Adsorbents and Microhydrated Complexes

To further refine the electronic characterization of the adsorbents and microhydrated metal complexes, a complementary analysis based on the ionization potential (I) and electron affinity (A) was introduced. These quantities were estimated from frontier orbital energies within the Koopmans approximation using the relationships $I = -E_{HOMO}$ and $A = -E_{LUMO}$ (Table 6). This approach enables a more transparent interpretation of each system's relative ability to donate or accept electron density, avoiding reliance solely on the HOMO–LUMO gap, whose magnitude can be strongly affected by the description of the virtual space, particularly by the energetic sensitivity of the LUMO. Within this framework, larger values of I indicate a greater resistance to electron removal, whereas more positive values of A suggest an enhanced capacity to stabilize additional electronic charge. Conversely, negative values of A indicate a low propensity for charge acceptance, consistent with positive-energy LUMO orbitals and poor orbital stabilization of the reduced state.

Table 6. Ionization potential (I) and electron affinity (A) estimated from HOMO and LUMO energies of the adsorbents and microhydrated metal complexes within the Koopmans approximation. Values in Hartree.

Sistema	(I) (M06-2X-D3)	(A) (M06-2X-D3)	(I) (ωB97X-D)	(A) (ωB97X-D)
CTS	0.26699	−0.07333	0.28925	−0.11376
CTS–COO^-	0.27041	0.02360	0.28669	0.00570
CTS–COOH	0.26686	0.00424	0.28372	−0.02549
CTS–SH	0.25809	−0.01699	0.30453	−0.05483
CTS–NH_3^+	0.28563	−0.07445	0.25404	−0.09101
$[Cd(H_2O)_5]^{2+}$	0.06537	−0.01153	0.09062	−0.05652
$[Pd(H_2O)_5]^{2+}$	0.07752	0.01086	0.09759	−0.03513
$[Hg(H_2O)_5]^{2+}$	0.08655	−0.02032	0.11635	−0.05939

From this standpoint, the methodological comparison between M06-2X-D3 and ωB97X-D was grounded on descriptors with more direct physicochemical meaning than absolute total energies, which, although useful for computational traceability, are not suitable for establishing functional superiority due to their explicit dependence on both the functional and the basis set. For the adsorbents, the I values indicate that ωB97X-D generally predicts greater stabilization of the occupied frontier state, particularly for CTS, CTS–COO^-, CTS–COOH, and CTS–SH, leading to slightly higher ionization potentials than M06-2X-D3. The only clear exception was CTS–NH_3^+, for which M06-2X-D3 yielded a higher I value, suggesting a distinct electronic response associated with the protonated amino group. Regarding electron affinity, CTS–COO^- exhibited positive values with both functionals, indicating that this microenvironment retains the highest propensity to accept electron density among the adsorbents. CTS–COOH showed an intermediate behavior, with a weakly positive electron affinity in M06-2X-D3 and a negative value in ωB97X-D, whereas CTS, CTS–SH, and CTS–NH_3^+ displayed negative A values, consistent with a lower stabilization of the added charge.

For the $[M(H_2O)_5]^{2+}$ complexes, both functionals preserved the same general trend: I values increased in the order Cd < Pd < Hg, indicating that the mercury complex is the least susceptible to ionization among the three microhydrated systems. However, ωB97X-D systematically predicted higher I values than M06-2X-D3, reinforcing the notion of a stronger stabilization of the occupied frontier orbital. In contrast, electron affinity showed greater sensitivity to the choice of functional. At the M06-2X-D3 level, only the Pd(II) complex exhibited a positive A value, whereas Cd(II) and Hg(II) retained negative electron affinities. Under ωB97X-D, all three complexes presented negative A values, indicating a less favorable stabilization of the incoming electron. Overall, these results demonstrate that, although both levels of theory preserve comparable qualitative trends, the description of electron-accepting capability is considerably more sensitive to the treatment of the virtual orbital space than the description of ionization. Consequently, the combined use of I and A provides a more nuanced interpretation of the relative electronic response of both adsorbents and metal complexes than that obtained exclusively from the HOMO–LUMO gap.

3.3. Final Set of Optimized Structures and Dominant Coordination Modes (N/O/S)

Figure 1 compiles the optimized geometries of the five adsorbent models (CTS, CTS–COO^-, CTS–COOH, CTS–NH_3^+, and CTS–SH), obtained at the ωB97X-D/LANL2DZ level and verified as true minima (0 imaginary frequencies). In the absence of continuum solvation, these structures represent the "intrinsic state" of the fragment: the resulting conformation is governed by the balance between polysaccharide-backbone flexibility and conformational closure induced by intramolecular interactions (primarily hydrogen bonding). Therefore, before complexation with $[M(H_2O)_5]^{2+}$, it is important to establish whether functionalization (–COO^-/–COOH/–NH_3^+/–SH) reorganizes the folding and, in particular, whether the functional group remains exposed or becomes partially "shielded" by the internal network of weak interactions.

Overall, the conformational parameters (Table 7) indicate that carboxymethylation tends to yield slightly more extended structures than the parent chitosan. In particular, CTS–COO^- exhibits the largest effective size (radius of gyration, Rg = 4.57 Å) and the greatest internal maximum dimension (Dmax = 14.60 Å), consistent with the idea that incorporation of an anionic motif and additional oxygen atoms favors a less compact geometry under non-solvated conditions. By contrast, CTS and CTS–SH display comparable and relatively compact conformations (Rg ≈ 4.25 Å and 4.24 Å, respectively), suggesting that thiolation introduces a soft donor site without drastically perturbing the folding of the polysaccharide "core".

Table 7. Conformational descriptors and vibrational verification of the adsorbent geometries (ωB97X-D/LANL2DZ). Rg: radius of gyration (Å); Dmax: maximum interatomic distance (Å); "Intramol. H-bonds": geometric count of intramolecular hydrogen bonds; νmin: lowest positive frequency (cm^{-1}), with zero imaginary frequencies in all cases.

System	N Átomos	(Rg) (Å)	(Dmax) (Å)	H-Bonds Intramol.	νmin (cm^{-1})
CTS	69	4.25	13.08	2	15.15
CTS–COO^-	74	4.57	14.60	2	15.86

Table 7. *Cont.*

System	N Átomos	(Rg) (Å)	(Dmax) (Å)	H-Bonds Intramol.	νmin (cm^{-1})
CTS–COOH	75	4.51	13.84	2	13.74
CTS–NH_3^+	70	4.42	13.37	4	8.38
CTS–SH	75	4.24	12.81	2	11.82

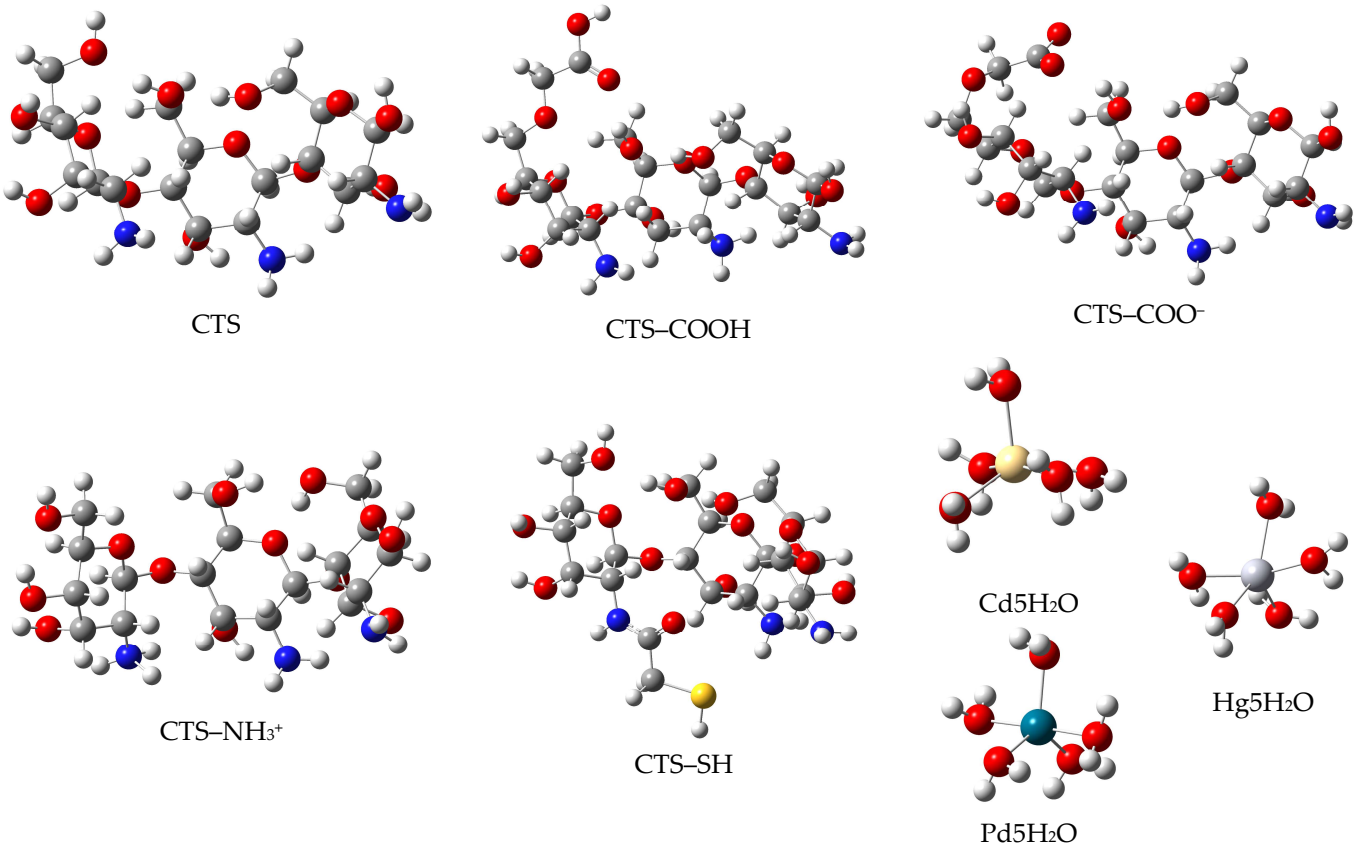


Figure 1. Optimized structures of the adsorbent models: CTS, CTS–COOH, CTS–COO^-, CTS–NH_3^+, and CTS–SH (DFT/ωB97X-D/LANL2DZ). Color code: C (gray), O (red), N (blue), S (yellow), H (white).

A particularly informative case is CTS–NH_3^+, where protonation increases the number of hydrogen-bond donors and strengthens the intramolecular network: the geometric count of intramolecular H-bonds increases (4 in CTS–NH_3^+ versus 2 in the other models). This reinforcement is accompanied by a lower minimum positive vibrational frequency (νmin = 8.38 cm^{-1}), indicative of soft torsional modes and substantial residual flexibility, as typically observed for polysaccharide fragments with many degrees of freedom. Mechanistically, this anticipates that upon formation of metal–biopolymer complexes, the protonated

environment may respond more sensitively to the approach of the pentahydrated metal (local reorganization via H-bonding), whereas in CTS–COO^- the dominant control is expected to be electrostatic and/or O-chelating in nature.

Figure 2 presents the optimized geometries of the CTS–Cd, CTS–Hg, and CTS–Pd complexes, computed at the ωB97X-D/LANL2DZ level of theory. A common structural feature across all three systems is that the hydrated cation fully retains its first coordination sphere as a penta-aqua complex; that is, the $[M(H_2O)_5]^{2+}$ unit remains 'closed', and no water-to-chitosan donor substitution is observed under these optimized geometrical conditions.

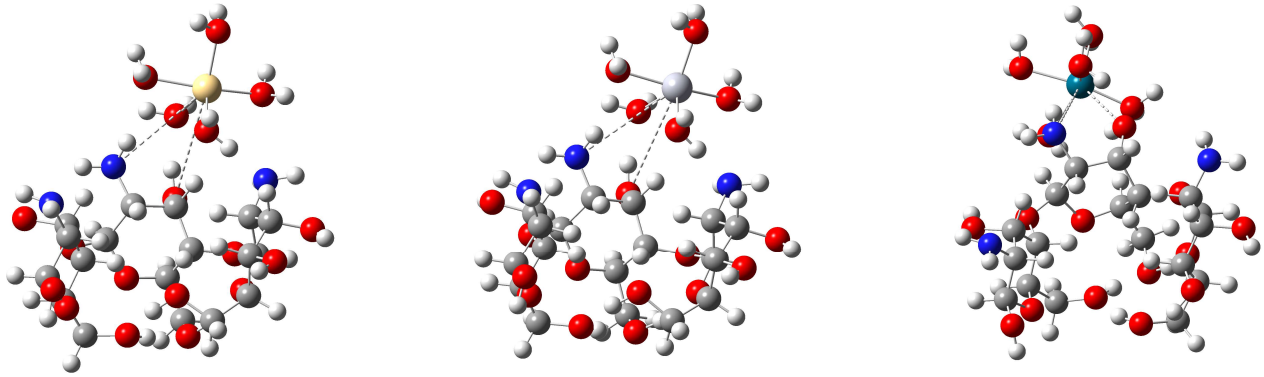


Figure 2. Optimized structures of the microhydrated CTS–Cd, CTS–Hg, and CTS–Pd complexes ($[M(H_2O)_5]^{2+}$) computed at the DFT/ωB97X-D/LANL2DZ level.

As summarized in Table 8, all optimized CTS–M adducts correspond to genuine minima on the potential energy surface and consistently preserve the first hydration shell of the metal center, as indicated by CNOw = 5 and k = 0 in all cases. The M–Ow distances remain within a compact range for Cd and Hg [2.077 ± 0.028 and 2.077 ± 0.032 Å, respectively]. At the same time, Pd shows a slightly broader distribution [2.083 ± 0.072 Å], but without loss of any coordinated water molecule. Thus, native chitosan does not induce ligand substitution at the primary coordination sphere of the microhydrated cation. This conclusion is reinforced by the metal···heteroatom separations, since the shortest contacts with chitosan remain outside a clear inner-sphere coordination regime, namely 3.703 Å for CTS–Cd, 3.689 Å for CTS–Hg, and 3.182 Å for CTS–Pd. Accordingly, the CTS–M interaction should be interpreted as an outer-sphere association governed primarily by electrostatic attraction, water-mediated coupling, and local second-sphere reorganization, rather than by direct donor coordination at the metal center.

Table 8. Structural parameters of optimized microhydrated CTS–M complexes (ωB97X-D/LANL2DZ). CNOw: number of first-sphere coordinated waters; k = 5 − CNOw; d(M–Ow) computed over the coordinated waters; d(M···X) denotes the shortest contact with a chitosan heteroatom (outer-sphere). All minima showed 0 imaginary frequencies.

Complex	CNOw	k	d(M–Ow) Min–Max (Å)	d(M–Ow) (Å)	X(CTS) Nearest	d(M···X) (Å)
CTS–Cd	5	0	2.027–2.100	2.077 ± 0.028	N	3.703
CTS–Hg	5	0	2.022–2.112	2.077 ± 0.032	N	3.689
CTS–Pd	5	0	1.973–2.185	2.083 ± 0.072	O	3.182

Table 8 also reveals a preference for a metal-dependent approach. For Cd and Hg, the nearest contact is with a nitrogen atom of chitosan, whereas for Pd, the closest approach is to oxygen. Although these differences do not support first-sphere coordination, they do indicate that the hydrated metal center responds to distinct local electrostatic environments

on the polymer surface. In this sense, native CTS acts mainly as a platform for outer-sphere associating, whose stability depends on the organization of the surrounding hydrated microenvironment rather than on systematic direct coordination.

Figure 3 compiles the optimized structures of CTS–COOH–Cd, CTS–COOH–Hg, and CTS–COOH–Pd. In all three cases, the metal remains as a penta-aqua species ($[M(H_2O)_5]^{2+}$), with no geometrical evidence of water substitution by biopolymer heteroatoms. Consequently, the dominant associating motif corresponds to an outer-sphere association, in which stabilization arises from long-range metal···(X) contacts and a hydrogen-bond network mediated by the coordinated water molecules.

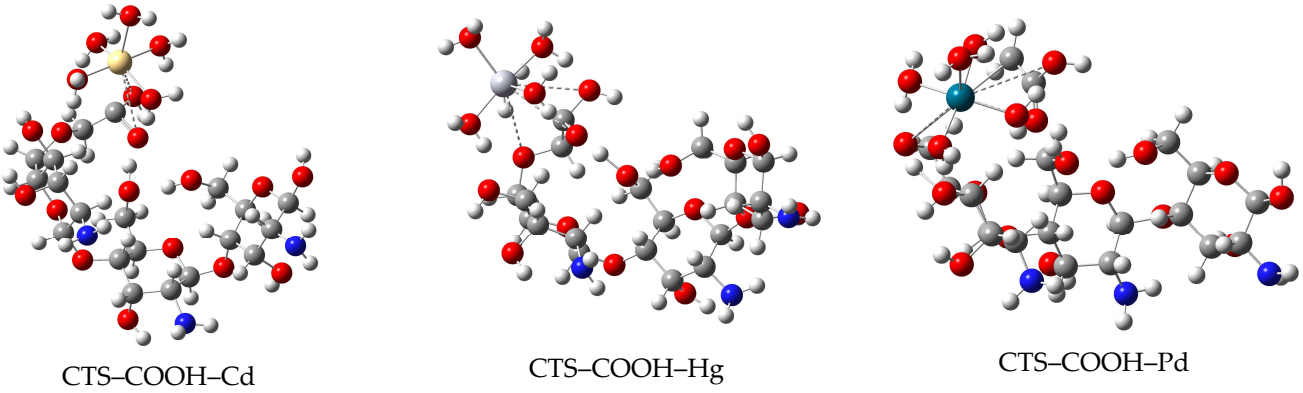


Figure 3. Optimized structures of the CTS–COOH–Cd, CTS–COOH–Hg, and CTS–COOH–Pd complexes (explicit microhydration with five water molecules), computed at the ωB97X-D/LANL2DZ level.

Structurally, the first hydration shell remains robust throughout the CTS–COOH series. For Cd, the Cd–Ow distances remain compact and close to those observed for native CTS, indicating that the neutral carboxylic motif does not displace coordinated water molecules or effectively compete for inner-sphere associating. A similar behavior is observed for Hg and Pd, where the hydrated cation remains intact, and the closest contacts with the biopolymer remain within a non-substitutive regime. Thus, the optimized geometries do not support water exchange or direct coordination of the protonated –COOH group at the metal center.

A mechanistically relevant effect of –COOH functionalization is instead the modification of the preferred region of approach of the hydrated metal toward the polymer. In the optimized structures, the nearest contacts shift toward oxygen-rich domains relative to native CTS, but this should not be interpreted as evidence of inner-sphere coordination by the carboxylic acid group itself. Rather, in its protonated state, –COOH appears to reorganize the local electrostatic environment and hydrogen-bonding network, thereby favoring outer-sphere stabilization through second-sphere interactions and conformational preorganization. Accordingly, the coordinating behavior typically associated with carboxylate sites should be reserved for the deprotonated $–COO^-$ form, rather than inferred from the CTS–COOH–M complexes (Table 9).

Table 9. Structural parameters of microhydrated CTS–COOH–M complexes (optimized geometries). CNOw: number of coordinated waters; k = 5 − CNOw; d(M–Ow) computed over coordinated waters; d(M···X) denotes the shortest contact with a biopolymer heteroatom (non-water).

Complex	CNOw	k	d(M–Ow) Min–Max (Å)	d(M–Ow) (Å)	X(CTS) Nearest	d(M···X) (Å)
CTS–COOH–Cd	5	0	2.029–2.101	2.077 ± 0.027	O	3.216
CTS–COOH–Hg	5	0	2.016–2.210	2.080 ± 0.068	O	3.371
CTS–COOH–Pd	5	0	1.984–2.381	2.094 ± 0.146	O	3.220

Figure 4 presents the optimized structures of CTS–COO^-–Cd, CTS–COO^-–Hg, and CTS–COO^-–Pd. In contrast to CTS and CTS–COOH (where outer-sphere association dominates), introduction of the carboxylate (–COO^-) increases the ability to 'anchor' the hydrated cation through electrostatic interaction and O-site preorganization. However, the behavior is strongly metal-dependent: only Cd shows geometrical evidence of incipient inner-sphere coordination with the carboxylate, whereas Hg remains within an outer-sphere regime.

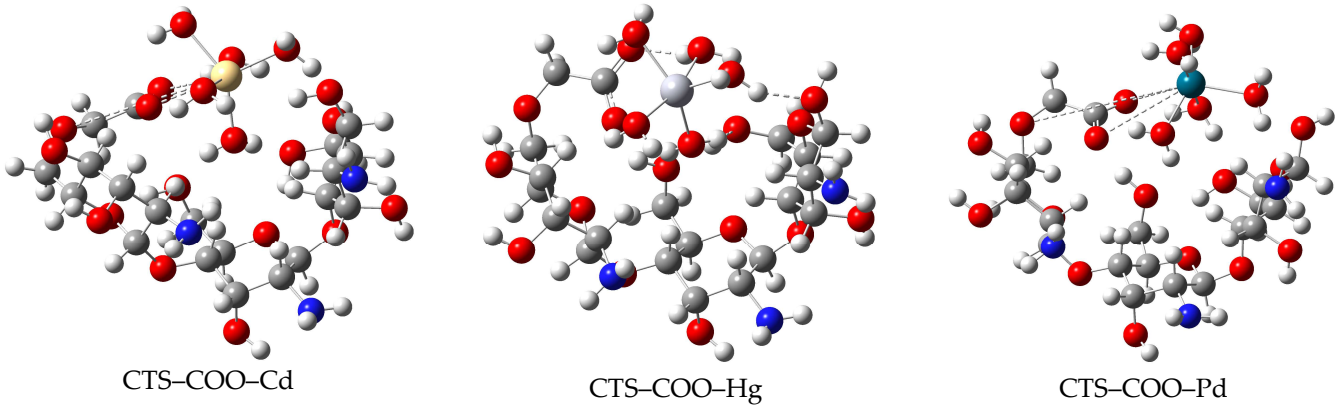


Figure 4. Optimized structures of the CTS–COO^-–Cd, CTS–COO^-–Hg, and CTS–COO^-–Pd complexes (explicit microhydration with five water molecules), computed at the ωB97X-D/LANL2DZ level.

In the CTS–COO^- series, the metal-dependent response becomes more clearly differentiated. For Cd, one carboxylate oxygen approaches the metal center to 2.658 Å, which is consistent with an incipient coordinative contact. However, because the five coordinated water molecules are still retained [d(Cd–Ow) = 2.040–2.097 Å; 2.076 ± 0.021 Å], this structure is more appropriately described as a partially inner-sphere or solvent-shared arrangement rather than as full ligand substitution. Thus, the carboxylate behaves as a strong anchoring region for Cd(II), promoting direct approach to the metal center while the optimized minimum still preserves the primary hydration shell.

By contrast, Hg and Pd remain in an outer-sphere regime in the optimized CTS–COO^- complexes. In both cases, the carboxylate contacts remain substantially longer, and no clear evidence of first-sphere water replacement is observed, while the hydrated metal core remains structurally preserved. These results indicate that the carboxylate does not affect all metals equally. Under the adopted microhydration model, it promotes a more direct and incipiently coordinative interaction for Cd(II). In contrast, for Hg(II) and Pd(II), their role is mainly to generate an anionic electrostatic anchoring site without consolidating systematic inner-sphere coordination (Table 10).

Table 10. Structural parameters of microhydrated CTS–COO^-–M complexes (optimized geometries; 0 imaginary frequencies). CN_Ow: number of first-sphere coordinated waters; k = 5 − CN_Ow. d(M–O_w) reports the range and the mean ± standard deviation (Å). d(M–O_carb) corresponds to the two metal–carboxylate oxygen distances.

Complex	CNOw	k	d(M–Ow) Min–Max (Å)	d(M–Ow) (Å)	d(M–Ocarb,1) (Å)	d(M–Ocarb,2) (Å)
CTS–COO^-–Cd	5	0	2.040–2.097	2.076 ± 0.021	2.658	3.486
CTS–COO^-–Hg	5	0	2.014–2.117	2.078 ± 0.038	3.274	3.551
CTS–COO^-–Pd	5	0	2.033–2.248	2.082 ± 0.084	3.562	3.834

Figure 5 summarizes the optimized geometries of CTS–NH_3^+–Cd, CTS–NH_3^+–Hg, and CTS–NH_3^+–Pd. The dominant feature across all three systems is unambiguous: the metal center retains its first hydration shell as a penta-aqua species (CNOw = 5), with no substitution by heteroatoms from the biopolymer. Accordingly, k = 0 in all cases, and the complexes correspond to an outer-sphere regime.

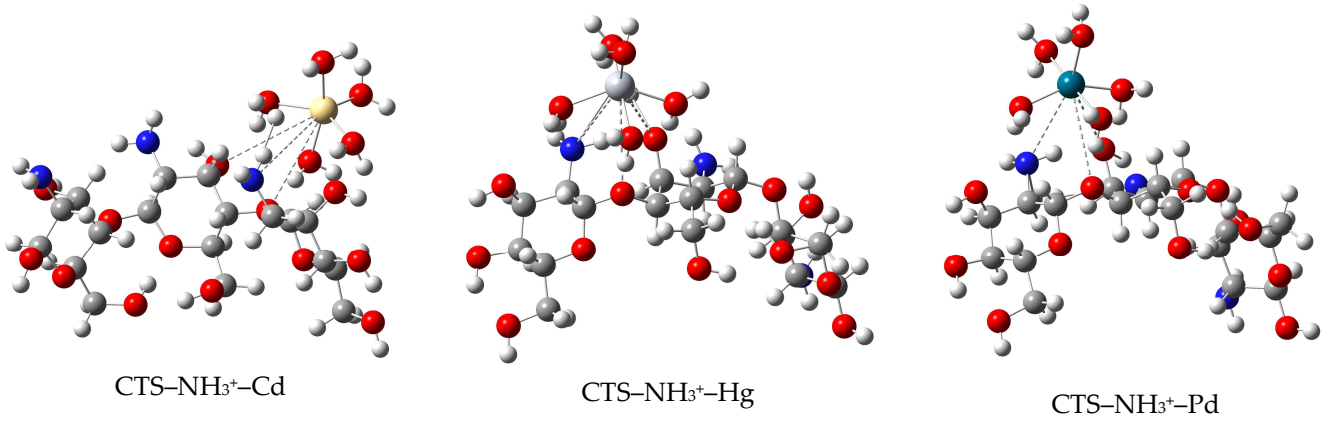


Figure 5. Optimized structures of the CTS–NH_3^+–Cd, CTS–NH_3^+–Hg, and CTS–NH_3^+–Pd complexes computed at the ωB97X-D/LANL2DZ level.

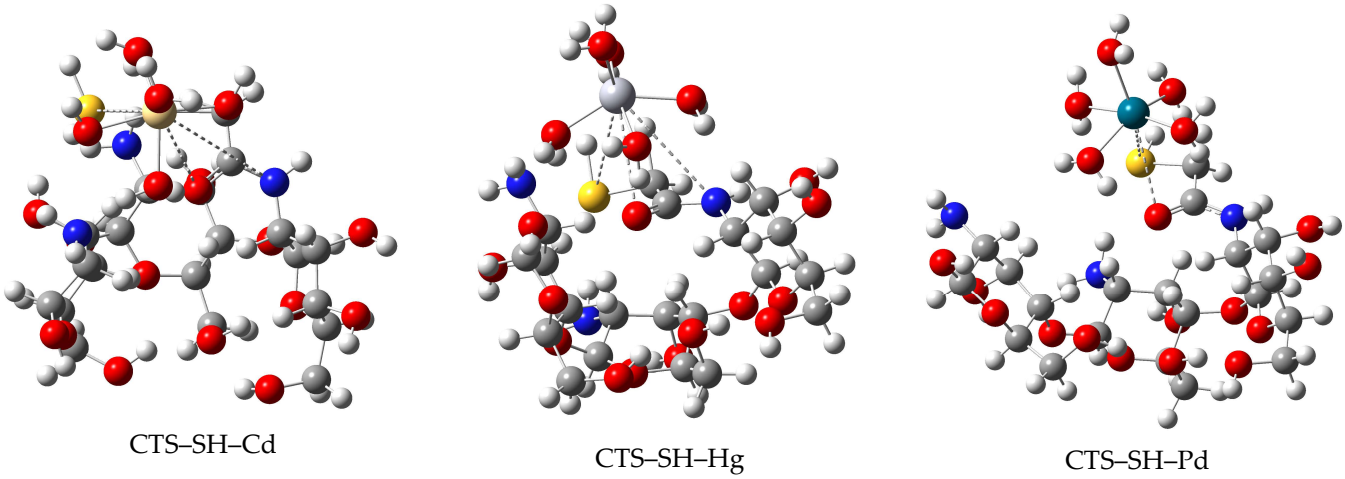
From a chemical standpoint, this behavior is consistent with protonation of the amino site. Because the –NH_3^+ group no longer provides a lone pair for direct donation, the protonated environment primarily serves as an electrostatic field modifier and organizer of the local hydrogen-bond network. Accordingly, the optimized minima correspond to outer-sphere association, in which the hydrated metal remains separated from the polymer donor atoms by the preserved water shell. Therefore, any stabilization gain observed for CTS–NH_3^+ should not be interpreted as direct nitrogen coordination. Instead, it reflects how protonation reshapes the local microenvironment, modifies the distribution of attractive regions on the adsorbent surface, and influences second-sphere organization around the hydrated cation.

Quantitatively (Table 11), the M–Ow distances remain compact and characteristic of a stable hydration sphere: Cd–Ow = 2.029–2.101 Å (2.077 ± 0.027 Å) and Hg–Ow = 2.027–2.134 Å (2.076 ± 0.037 Å). At the same time, the closest contact to the biopolymer occurs at long distances, particularly in CTS–NH_3^+–Cd, where the metal is notably farther from the adsorbent (d(Cd···O) = 4.015 Å), suggesting an even more strongly solvated association than in the neutral CTS or CTS–COOH complexes. For CTS–NH_3^+–Hg, the minimum contact (3.314 Å) remains consistent with an outer-sphere regime, reflecting that Hg(II) does not find in –NH_3^+ a site competitive with water. This anticipates that a transition toward genuine inner-sphere coordination for Hg(II) should arise from soft donors (e.g., –SH) or strongly anionic sites (–COO^-) under appropriate conditions.

Table 11. Structural parameters of microhydrated CTS–NH_3^+–M complexes (ωB97X-D/LANL2DZ). CNOw: number of waters coordinated to the metal; k = 5 − CNOw. d(M–Ow) is reported as range and mean ± standard deviation. d(M···X) corresponds to the shortest contact with a biopolymer heteroatom (excluding water oxygens).

Complex	CN(Ow)	k	d(M–O(_w)) Min–Max (Å)	d(M–Ow) (Å)	X(CTS) Nearest	d(M···X) (Å)
CTS–NH_3^+–Cd	5	0	2.029–2.101	2.077 ± 0.027	O	4.015
CTS–NH_3^+–Hg	5	0	2.027–2.134	2.076 ± 0.037	O	3.314
CTS–NH_3^+–Pd	5	0	1.993–2.322	2.089 ± 0.119	O	3.258

Figure 6 shows the optimized geometries of the CTS–SH–Cd, CTS–SH–Hg, and CTS–SH–Pd complexes. In this series, despite incorporating a soft sulfur donor, the dominant structural outcome is that the metal retains its first hydration shell as a penta-aqua species; that is, the $[M(H_2O)_5]$ fragment remains intact, and the thiol group displaces no water molecules. Accordingly, the microhydration parameters remain CNOw = 5 and k = 0 for the three complexes (Table 12), and the associated motif corresponds to an outer-sphere association.



CTS–SH–Cd CTS–SH–Hg CTS–SH–Pd

Figure 6. Optimized structures of CTS–SH–Cd, CTS–SH–Hg, and CTS–SH–Pd, computed at the ωB97X-D/LANL2DZ level. Dashed lines indicate metal···heteroatom contacts with the biopolymer.

Table 12. Structural parameters of optimized microhydrated CTS–SH–M complexes (ωB97X-D/LANL2DZ).

Complex	CN(Ow)	k	d(M–Ow) Min–Max (Å)	d(M–O(_w)) (Å)	d(M···S) (Å)	Minimal Contact with Biopolymer	νmin (cm^{-1})
CTS–SH–Cd	5	0	2.029–2.101	2.077 ± 0.027	3.594	O (3.582 Å)	8.0
CTS–SH–Hg	5	0	2.014–2.172	2.079 ± 0.052	4.089	O (3.395 Å)	131.7
CTS–SH–Pd	5	0	2.013–2.223	2.081 ± 0.074	3.341	O (3.280 Å)	140.4

This result indicates that the sulfur-containing derivative does not promote systematic first-sphere water substitution in the optimized minima discussed here. The thiol group remains in its neutral form, and the M···S distances are too long to support a clear inner-sphere M–S bond within this model. Consequently, the favorable thermodynamics calculated for some metals in the CTS–SH series should not be interpreted as proof of direct sulfur coordination in every case.

Instead, the role of the thiolated derivative is better understood in terms of a sulfur-containing polarizable microenvironment. The presence of sulfur modifies the local elec-

tronic response of the adsorbent. It can strengthen metal association through induced polarization, electrostatic anisotropy, and cooperative second-sphere interactions, even when the first hydration shell remains intact.

In addition, the aqueous shell exhibits different degrees of "deformability" depending on the metal: Cd shows a very compact first coordination sphere ($\sigma \approx 0.027$ Å), whereas Hg and Pd display larger dispersion in M–Ow distances ($\sigma \approx 0.052$–0.074 Å), consistent with a more flexible hydrated environment. However, this flexibility does not translate into M–S bond formation. In fact, the shortest non-aqueous contact in all three complexes involves an oxygen atom from the biopolymer (3.28–3.58 Å), confirming that even the approach toward sulfur does not geometrically dominate the assembly in the isolated phase (Table 12).

3.4. Biosorption Thermodynamics: Affinity and Selectivity (ΔEassoc/ΔGassoc)

In this section, association free energies (ΔGassoc) are discussed as the thermodynamic metric for comparing relative metal affinities across functional groups within the adopted explicit microhydration framework. More negative ΔGassoc values indicate a more favorable formation of the hydrated metal–adsorbent adduct. Because most optimized structures retain the metal's primary hydration shell, these values should be interpreted as descriptors of comparative stabilization of microhydrated assemblies rather than as direct measures of systematic first-sphere ligand substitution. Accordingly, relative differences between materials for a given metal, and between metals for a given material, are used here to discuss selectivity trends (Table 13).

Table 13. Calculated associating energies (ΔGassoc) for the adsorption of Cd, Hg, and Pd on CTS and its functionalized derivatives (–COOH, $–COO^-$, $–NH_3^+$, and –SH). Values are reported in kcal·mol^{-1}.

Adsorbent	Cd	Hg	Pd
CTS	−37.3	−30.0	−99.1
CTS–COOH	−90.0	−37.9	−48.4
CTS–COO^-	−54.4	−52.9	−67.5
CTS–NH_3^+	−58.7	−65.2	−88.9
CTS–SH	−46.1	−87.0	−90.0

For Cd(II), the calculated trend indicates that the CTS–COOH microenvironment provides the most favorable stabilization within the present model, clearly outperforming native CTS and the remaining functionalizations. This result suggests that the acidic carboxylic environment promotes a particularly favorable organization of the hydrated metal–polymer assembly. Importantly, this trend should not be interpreted as evidence that the protonated carboxylic group systematically behaves as a stronger direct ligand than the carboxylate. Rather, the data support a cooperative mechanism in which conformational preorganization, local electrostatic directionality, and second-sphere interactions contribute significantly to the calculated free-energy gain.

For Hg(II), the most favorable calculated association is obtained for the thiolated derivative, followed by CTS–NH_3^+ and CTS–COO−, whereas CTS and CTS–COOH are comparatively less favorable. This trend indicates that Hg(II) is especially sensitive to the electronic character and polarizability of the local microenvironment. However, because the optimized CTS–SH–Hg structure retains the primary hydration shell and does not show a short inner-sphere Hg–S bond, the observed stabilization is better attributed to the sulfur-containing polarizable environment than to systematic direct sulfur coordination. In this sense, thiolation appears to "program" a favorable microenvironment for Hg(II) association within the adopted computational scheme.

Pd(II) displays the most distinctive behavior in the present series, with native CTS providing the most favorable calculated association free energy, followed closely by CTS–SH and CTS–NH_3^+. In contrast, carboxylic functionalization significantly reduces stabilization. This result indicates that Pd(II) responds differently to local chemical modification than Cd(II) and Hg(II), and that introducing additional charge or donor groups does not necessarily improve its affinity within the adopted model. Because Pd(II) is particularly sensitive to coordination environment and speciation, these results should be interpreted comparatively and supported by the subsequent electronic and noncovalent interaction analyses rather than as a universal prediction independent of solution conditions.

When selectivity is analyzed by adsorbent (metal competition on the same material), three clear design rules emerge. Native CTS is strongly selective toward Pd(II) (Pd $\ll$ Cd $\approx$ Hg in ΔG_{assoc}), positioning it as a baseline platform for Pd capture in the presence of other cations. CTS–COOH directs selectivity toward Cd(II), with a large thermodynamic separation relative to Hg(II) and Pd(II), and thus behaves as a "Cd-specific" adsorbent under the modeled conditions. CTS–SH is essentially co-selective for Hg(II) and Pd(II) (difference ~3 kcal·mol^{-1}) and strongly discriminates against Cd(II), which is particularly advantageous when Cd acts as an interferent. CTS–COO^- and CTS–NH_3^+ occupy an intermediate regime: they increase affinity for Hg(II) and Cd(II) relative to CTS. Yet, they retain an overall preference for Pd(II), suggesting a preference for "polyvalent" materials with moderate selectivity.

3.5. Electrostatic Origin of Preference: ESP/MEP Analysis

Because most optimized complexes retain the first hydration sphere of the metal, the ESP/MEP analysis is interpreted here primarily as a descriptor of induced polarization and electrostatic organization of the adsorbent microenvironment, rather than as direct proof of inner-sphere metal–heteroatom coordination. In Figure 7, CTS exhibits moderate anisotropy in the potential: the most negative regions are concentrated around oxygen-bearing heteroatoms (electron-density-rich sites), whereas the positive regions are associated with relatively electron-poor domains (notably environments enriched in polar hydrogens). This "baseline" pattern is consistent with capture dominated by outer-sphere interactions and second-sphere stabilization, in which the metal preferentially positions itself near accessible negative patches, and the complex is stabilized through local microenvironment reorganization.

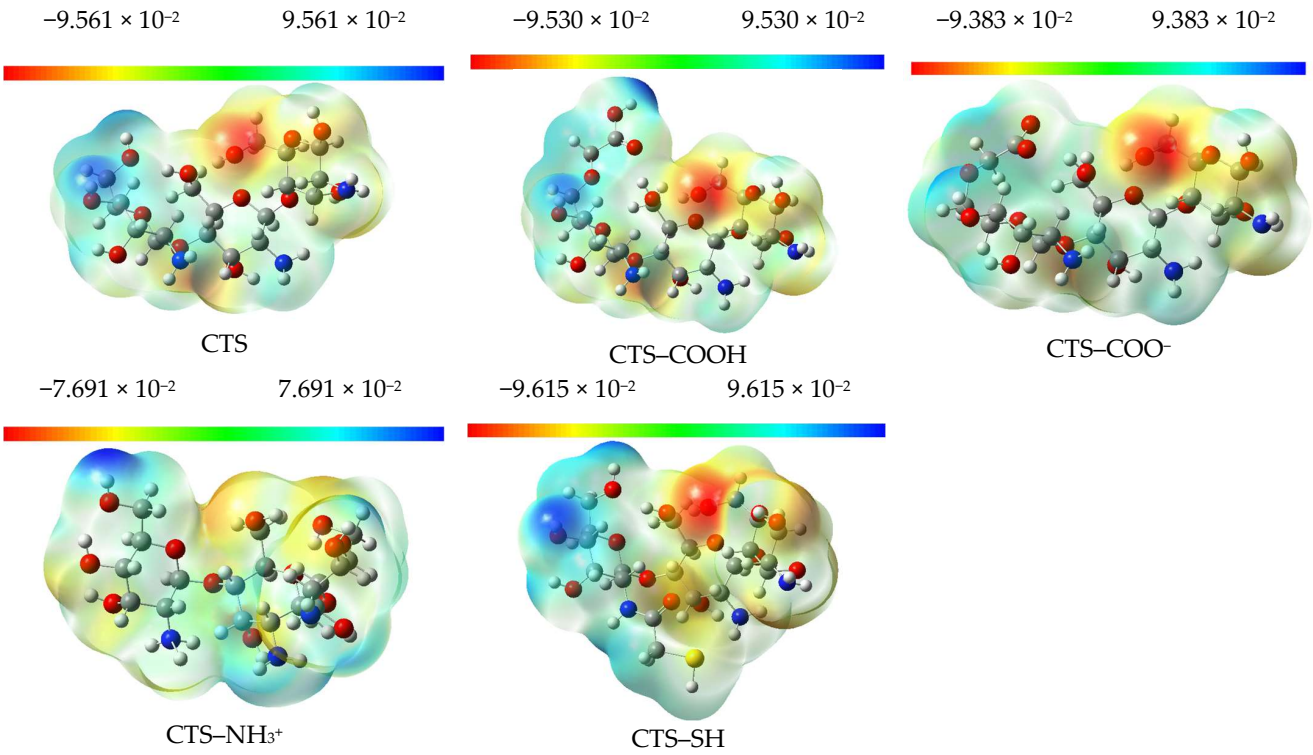


Figure 7. ESP/MEP maps mapped onto the molecular surface of CTS and its derivatives (–COOH, $–COO^-$, $–NH_3^+$, and –SH); red denotes more negative potential and blue more positive potential (scale in a.u.).

Carboxylic functionalization introduces a more directional electrostatic signature. In CTS–COOH, the acidic group generates a local dipole (oxygen atoms with more negative potential coexisting with a relatively positive proton), producing a heterogeneous patch that can stabilize cation approach through a combination of attraction toward the oxygen atoms and coupling to the surrounding hydrogen-bond network. This point is relevant because it anticipates that the thermodynamic preference observed for Cd(II) on CTS–COOH does not necessarily correlate linearly with "more negative charge", but rather with the site's ability to organize cooperative interactions (electrostatics + H-bonding) around the cation.

In CTS–COO^-, the carboxylate increases both the intensity and spatial continuity of negative regions around the $–COO^-$ motif, generating a more pronounced electrostatic attractor for positively charged species. However, while this scenario favors initial Coulombic anchoring, it may also entail (depending on the metal and the explicit microenvironment) a higher energetic cost associated with reorganization/desolvation or with the loss of specific hydrogen-bond stabilization present in –COOH. Thus, within the thermodynamic results framework, the MEP supports the notion that selectivity is not purely electrostatic, but rather "contextual" electrostatics modulated by the final geometry and second-sphere stabilization.

The ammonium state CTS–NH_3^+ exhibits a distinctive pattern: an electropositive domain associated with the protonated group is evident (consistent with suppression of direct donation from the N lone pair), accompanied by residual negative patches in oxygen-rich regions. Moreover, the displayed potential range is comparatively narrower, compatible with partial "screening" of the overall electrostatic contrast. In terms of affinity, this pattern supports an interpretation in which $–NH_3^+$ acts primarily as a field modulator and microenvironment organizer (e.g., promoting hydration arrangements and indirect stabilization) rather than as a hard first-sphere coordinating site.

Finally, CTS–SH preserves a high anisotropy in the potential, with a characteristic contribution from the sulfur-containing environment: sulfur does not necessarily generate the most negative patch, but it does contribute a spatially diffuse, highly polarizable domain. This is consistent with a preference for soft/polarizable cations (such as Hg) that cannot be explained solely by MEP magnitude.

Upon complex formation (CTS–COOH–M, CTS–COO^-–M, CTS–NH_3^+–M, and CTS–SH–M), the ESP/MEP maps reveal clear induced polarization (Figure 8): the potential becomes markedly electropositive in the immediate vicinity of the cation (blue lobe), while the most electronegative regions intensify over the heteroatoms of the anchoring site (red–yellow zones). This spatial separation of potentials constitutes the "electrostatic fingerprint" of complexation: the metal imposes a strong field, and the adsorbent responds by redistributing electron density and orienting polar groups within the local microenvironment.

A useful indicator here is the scale range ($|V|_{max}$) for each complex. For CTS–COOH–M, the ranges are on the order of ± 0.12 a.u., reflecting a relatively high polarization that is, importantly, well localized around the carboxylic motif. This pattern is consistent with a site that behaves as a structured dipole (C=O/–OH) capable of stabilizing the cation not only through attraction toward oxygen atoms, but also through cooperative coupling with the hydrogen-bond network (second sphere). In other words, the "electrostatic origin" here is not merely net charge, but directionality and microenvironment preorganization.

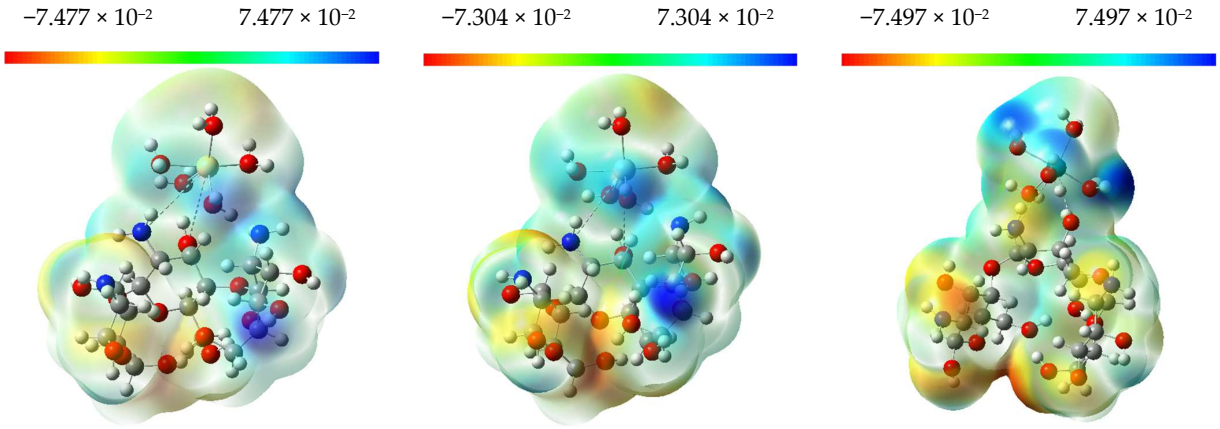


Figure 8. *Cont.*

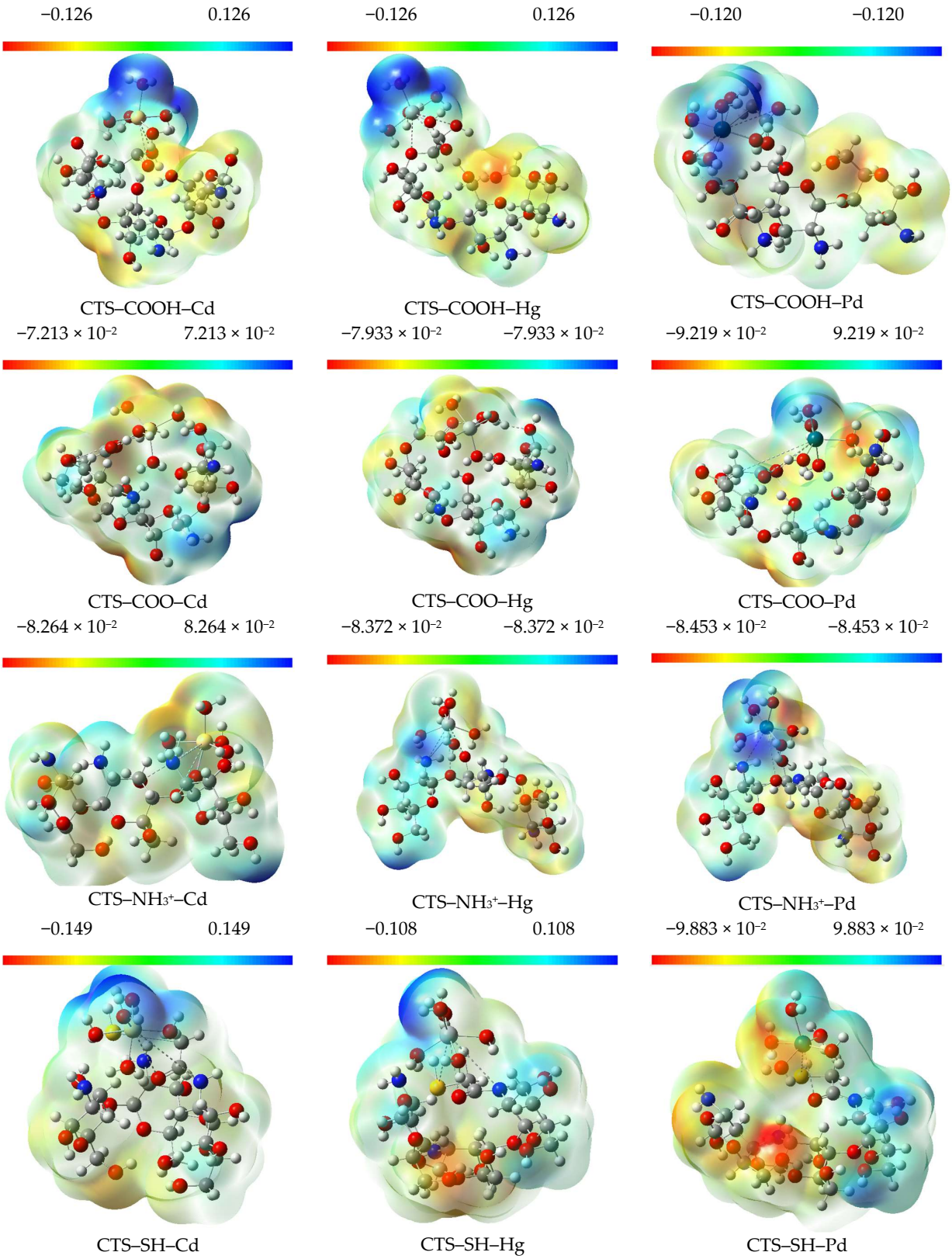


Figure 8. ESP/MEP maps of the CTS–COOH–M, CTS–COO^-–M, CTS–NH_3^+–M, and CTS–SH–M complexes (M = Cd, Hg, Pd) mapped onto the molecular surface; red denotes more negative potential and blue more positive potential (scale in a.u.).

In CTS–COO^-–M, the ranges decrease to ~(0.07–0.09) a.u., and the negative potential becomes more spatially extended over the carboxylate and nearby oxygens, suggesting a

less "focal" and more distributed electrostatic attractor. This type of signature typically favors the initial Coulombic interaction between the cation and the ligand. Yet, it can translate into only moderate thermodynamic stabilization if the final complex remains governed by reorganization/hydration (especially when first-sphere coordination is not consolidated). Put differently, a broader electrostatic well does not, by itself, guarantee the deepest minimum in ΔGassoc; the final geometry and second-sphere stabilization remain decisive.

For CTS–NH_3^+–M, the maps exhibit a persistent electropositive domain associated with the ammonium group and intermediate ranges (~±0.083–0.085 a.u.). The key point is that the metal cation does not "compete" with the ammonium as a direct donor; rather, N protonation reshapes the global electrostatic landscape (a field effect), shifting and organizing attractor regions around oxygenated and other polar groups. This supports a mechanistic interpretation in which –NH_3^+ contributes primarily as a microenvironment (and second-sphere) modulator, rather than as a classical lone-pair coordination center.

Finally, CTS–SH–M shows the most pronounced electrostatic contrast for Cd (±0.149 a.u.) and still-elevated ranges for Hg and Pd (≈±0.108 and ±0.0988 a.u.). This increased contrast is consistent with the high polarizability of the sulfur-containing motif: the site can generate a strong electrostatic response to the cationic field even if the local formal "charge" is not extreme. This result is particularly important for Hg and Pd because it suggests that preference is not explained solely by static electrostatics, but by induced polarization of the site (which commonly correlates with a larger specific contribution from metal–site interactions).

3.6. Acid–Base Modeling: Protonation States and Charge Consistency

As summarized in Table 13, the results confirm that protonation state modulates metal affinity not only through formal charge, but also through changes in donor availability, electrostatic directionality, and local hydration organization. Within the present microhydrated model, Cd(II) is most strongly stabilized in the CTS–COOH environment, Hg(II) is preferentially favored by the sulfur-containing CTS–SH derivative, and Pd(II) remains most stabilized by native CTS and other non-carboxylic environments. These trends indicate that the protonation state determines the material's capture profile within the local coordinating microenvironment.

At the same time, these results should not be interpreted as a direct representation of experimental pH-dependent speciation. Rather, the selected acid–base forms are used here as comparative states to evaluate how local protonation perturbs metal association under a controlled computational framework with explicit microhydration. In this sense, the observed selectivity arises from the combined effects of protonation state, site accessibility, and second-sphere organization, rather than from formal charge alone. Therefore, charge consistency across the compared models remains essential for interpreting relative ΔGassoc values.

3.7. Secondary Interactions and the Role of Microhydration: NCI/RDG

To clarify the physical origin of stability beyond the electrostatic term, noncovalent interactions were evaluated using the NCI formalism by representing RDG as a function of sign(λ_2)P for the CTS–M complexes and the functionalized materials (Figure 9). Within this framework, negative sign(λ_2)P values are associated with attractive (stabilizing) regions, values near zero reflect dispersive van der Waals contacts, and positive values correspond to steric (Pauli) repulsion. Overall, the plots exhibit a consistent pattern: the dominant contribution is centered on sign(λ_2)P ≈ 0, indicating that global complex stabilization is strongly influenced by dispersive interactions and microenvironment packing, in line with

a biosorption mechanism in which the second sphere (local reorganization and multiple weak contacts) is structurally relevant.

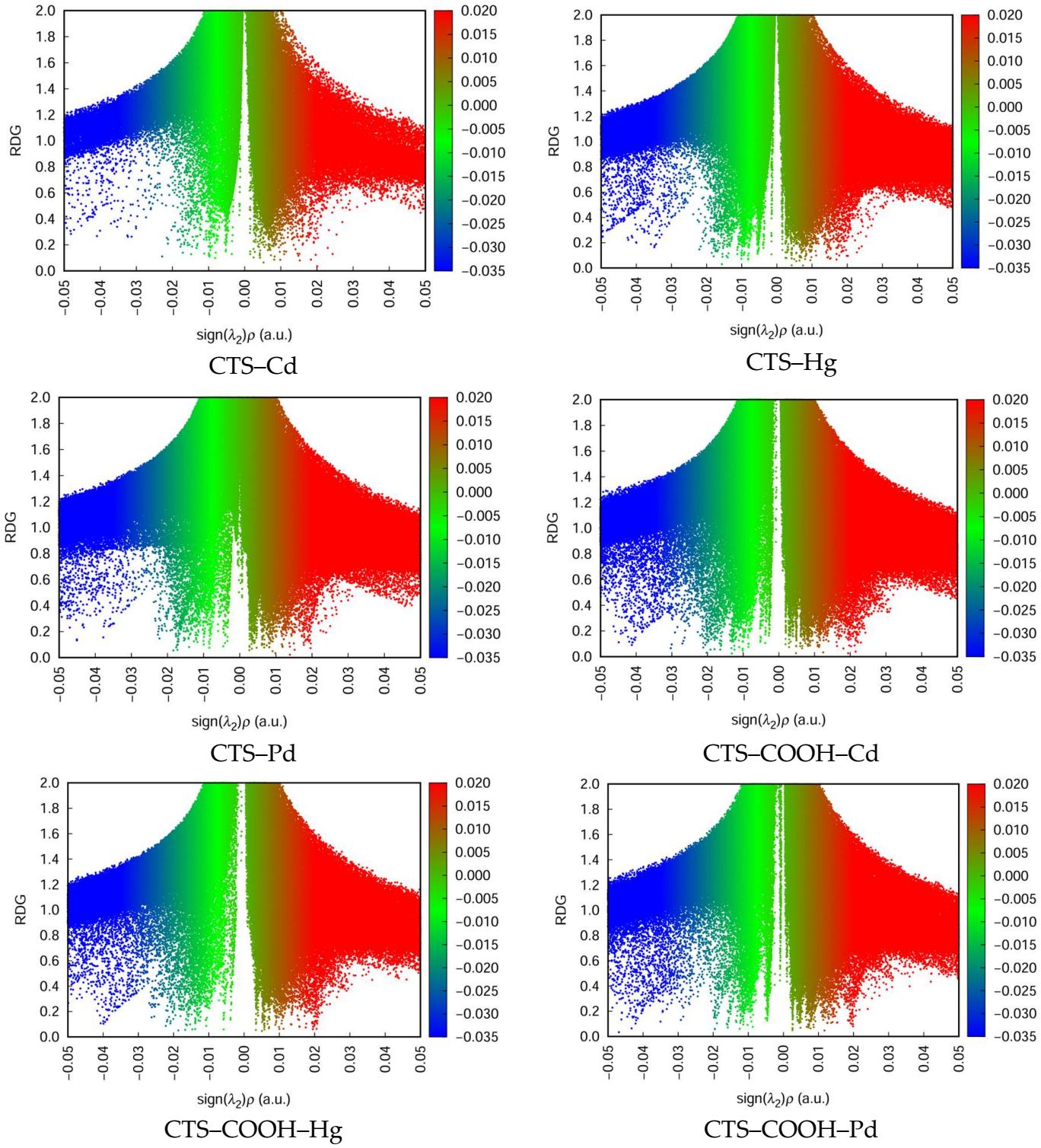


Figure 9. *Cont.*

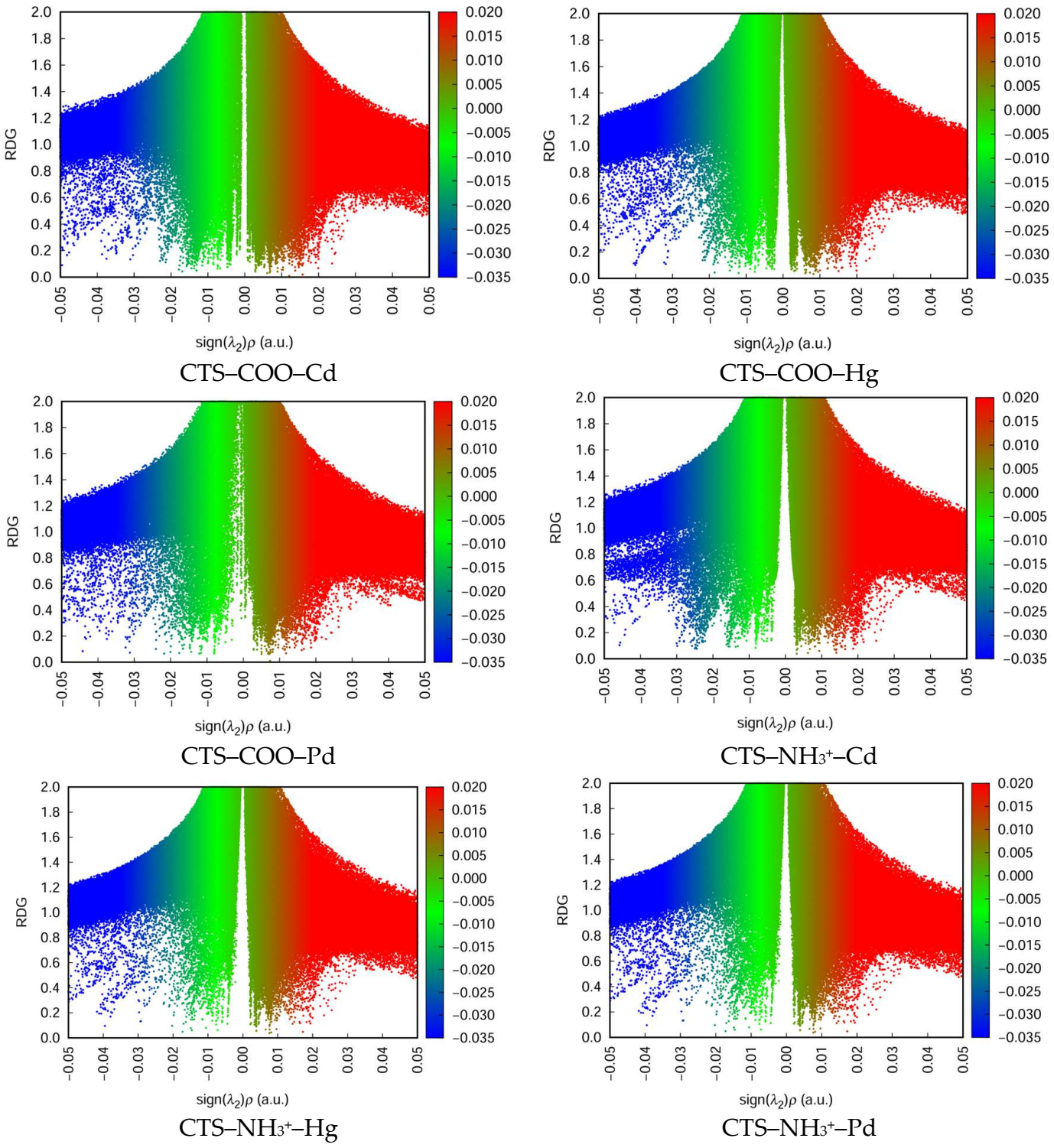


Figure 9. *Cont.*

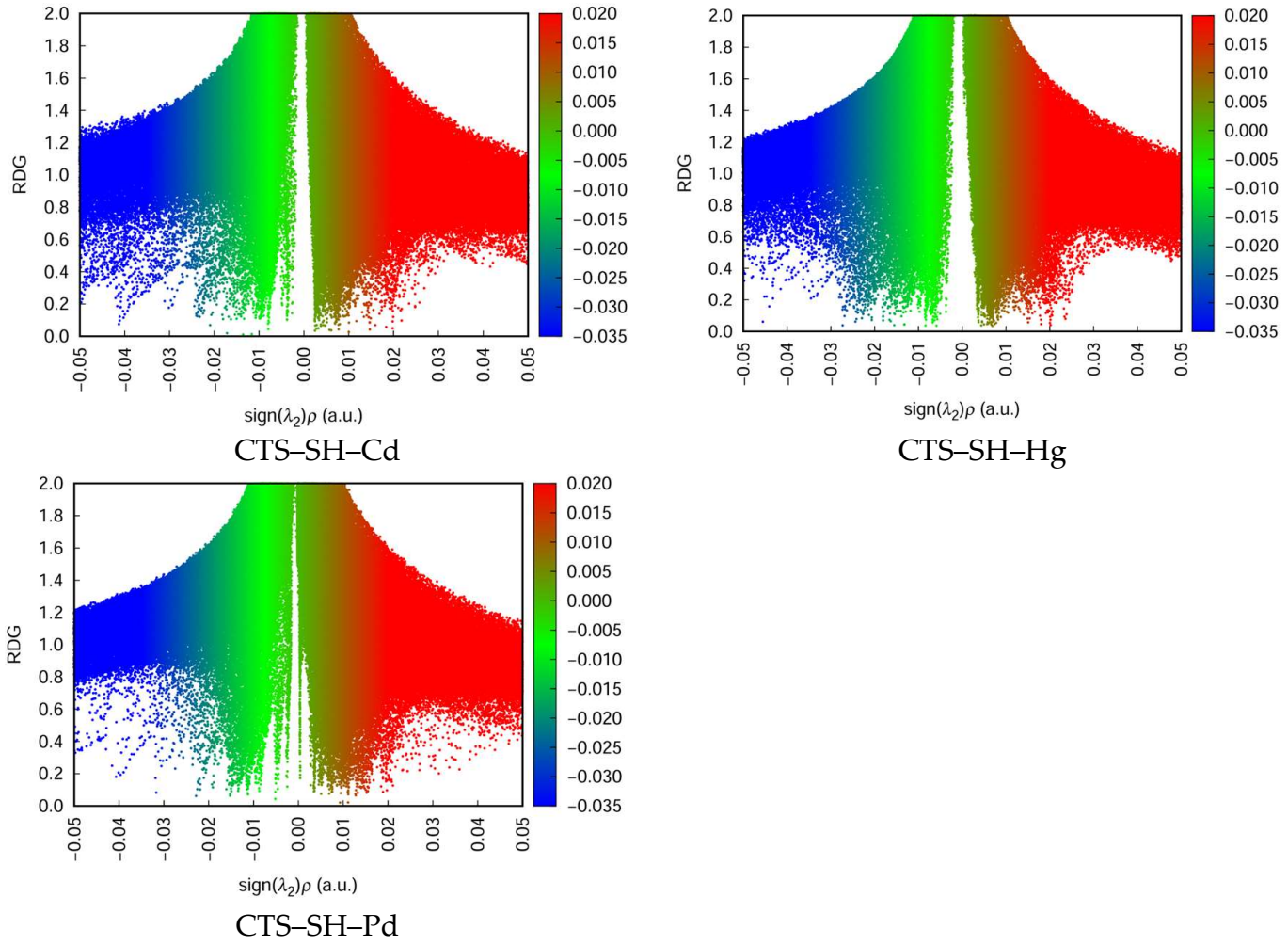


Figure 9. NCI plots (RDG vs. sign(λ_2)P) for CTS and its derivatives complexed with Cd, Hg, and Pd; sign(λ_2)P < 0 indicates attractive interactions, ≈0 dispersive contacts, and >0 steric repulsion.

For the non-functionalized CTS complexes (CTS–Cd, CTS–Hg, and CTS–Pd), the point cloud shows an appreciable contribution in the negative domain, but without a pronounced shift toward very negative sign(λ_2)P values. This suggests that, although attractive metal–environment regions exist, the interaction is not dominated by a single highly directional contact; instead, it reflects a set of distributed, moderate contributions (long-range electrostatics, dispersion, and polarization). The fact that the overall pattern is similar across Cd, Hg, and Pd further supports that, in the parent material, selectivity does not originate from an isolated "strong bond", but rather from how each metal reorganizes the polar environment of the biopolymer.

Introducing the carboxylic group perturbs the balance between attractive/repulsive forces without altering the predominantly noncovalent character of the coupling. In CTS–COOH–M, the density of points in the negative region becomes more marked and more continuous around mildly negative values, consistent with additional second-sphere attractive interactions (e.g., hydrogen bonds and polarized contacts) around the acidic site. This outcome is particularly consistent with the high thermodynamic affinity observed for Cd(II) on CTS–COOH: the NCI signature indicates that stabilization need not arise from enforcing strongly covalent inner-sphere coordination, but can emerge from a cooperative network of weak interactions that, in aggregate, deepens ΔGassoc. By contrast, the carboxylate form (CTS–COO^-–M) retains the near-zero dispersive domain as the dominant contribution and shows a more "diffuse" attraction (sign(λ_2)P < 0), consistent with a more extended

electrostatic attractor that is less focalized into specific contacts; this can rationalize why, despite a higher formal charge, it does not necessarily maximize free-energy stabilization for all metals.

In the CTS–NH_3^+–M systems, the presence of ammonium reinforces the "microenvironment" interpretation: the central van der Waals (vdW) contribution is preserved, and a moderate attractive contribution appears in the negative domain, yet without evidence of a shift toward extremely strong interactions. In other words, the protonated group primarily organizes the interaction landscape (electrostatic field + H-bond network) rather than serving as a direct coordination center. This point is methodologically important because it prevents an incorrect interpretation of the type "protonated N coordinates": the NCI signature indicates that any observed stability gain arises from cooperative rearrangement of the surrounding environment.

Overall, the NCI analysis indicates that the calculated selectivity does not arise from an all-or-nothing distinction between covalent and noncovalent binding. Instead, stabilization emerges from a cooperative balance of multiple moderate attractions, persistent dispersive contributions, and local reorganization of the hydrated interface. This interpretation is fully consistent with the optimized geometries, in which most systems retain the metal's primary hydration shell and therefore behave predominantly as outer-sphere assemblies, with varying degrees of second-sphere stabilization.

3.8. Comparison with Experimental Literature

The calculated trends are qualitatively consistent with several experimental observations reported for chitosan-based adsorbents. However, the correspondence should be interpreted with caution because the present calculations employ a simplified microhydrated cation model. In the case of Hg(II), thiolated chitosan materials have been experimentally reported to display enhanced mercury uptake relative to non-thiolated chitosan, supporting the idea that sulfur-containing modification promotes a favorable chemical environment for Hg capture [7,20]. In the present calculations, this favorable behavior is expressed as a stronger association of Hg(II) with CTS–SH, although the optimized structures indicate that the effect is mainly mediated by a polarizable sulfur-containing microenvironment and second-sphere stabilization rather than by systematic direct Hg–S bond formation.

For Cd(II), previous experimental studies on carboxymethylated chitosan have shown that introduction of carboxylic/carboxylate functionality improves the interaction with divalent metal ions and can enhance adsorption performance relative to native chitosan [8,21]. This experimental background is qualitatively consistent with the present prediction that the carboxylic microenvironment strongly favors Cd(II) association. However, the specific result that the protonated CTS–COOH model is thermodynamically more favorable than CTS–COO− should be regarded as a model-dependent outcome that still requires direct experimental verification.

For Pd(II), both native and modified chitosan-based materials have been experimentally explored for selective palladium recovery [9,22]. The present calculations predict a particularly favorable association for native CTS. Still, this trend should be interpreted cautiously because the real aqueous speciation of Pd(II) depends strongly on solution composition and may differ substantially from the simplified cationic microhydration scheme used here. Therefore, the strongest value of the present study lies in defining relative electronic and microenvironmental trends that can guide future experimental validation under controlled pH, ionic strength, and ligand conditions.

4. Conclusions

Within the explicit microhydration framework adopted in this work, the calculated association free energies reveal clear metal-dependent affinity regimes for native and functionalized chitosan models. The results suggest that the carboxylic microenvironment is the most favorable for Cd(II), the sulfur-containing derivative provides the most favorable association for Hg(II), and native CTS affords the strongest calculated stabilization for Pd(II). These trends indicate that functionalization reshapes the adsorption profile of chitosan in a metal-specific and non-monotonic manner.

The optimized geometries show that, in most cases, the metal's first hydration shell is preserved. Accordingly, the dominant stabilization mechanism should be interpreted mainly in terms of outer-sphere association, induced polarization, and cooperative second-sphere interactions rather than as systematic first-sphere ligand substitution. This interpretation is supported by the ESP/MEP maps, which reveal heterogeneous and directional electrostatic attractor regions, and by the NCI analysis, which shows that stabilization arises from the cumulative effect of dispersive and moderately attractive weak interactions.

Therefore, the most robust outcome of the present study is the relative hierarchy of affinities and the identification of chemically distinct microenvironments that can favor different metals under a controlled comparative model. Because absolute energetic values may depend on the simplified hydration treatment, conformational sampling, and the real aqueous speciation of each metal, these results should be regarded as testable mechanistic hypotheses that can guide future experimental validation under controlled solution conditions.

Author Contributions: Conceptualization, J.H.-F., R.G.-C. and R.O.-T.; Methodology, J.H.-F.; Software, J.H.-F. and R.O.-T.; Validation, J.H.-F. and R.G.-C.; Formal analysis, J.H.-F., R.G.-C. and R.O.-T.; Investigation, J.H.-F., R.G.-C. and R.O.-T.; Resources, J.H.-F. and R.G.-C.; Data curation, J.H.-F.; Writing—original draft, J.H.-F., R.G.-C. and R.O.-T.; Writing—review & editing, J.H.-F.; Visualization, J.H.-F., R.G.-C. and R.O.-T.; Supervision, J.H.-F.; Project administration, J.H.-F.; Funding acquisition, J.H.-F. All authors have read and agreed to the published version of the manuscript.

Funding: This research received no external funding.

Institutional Review Board Statement: Not applicable.

Informed Consent Statement: Not applicable.

Data Availability Statement: The original contributions presented in this study are included in the article. Further inquiries can be directed to the corresponding author.

Acknowledgments: To the University of Cartagena for your support.

Conflicts of Interest: The authors declare no conflicts of interest.

References

1. Briffa, J.; Sinagra, E.; Blundell, R. Heavy metal pollution in the environment and its toxicological effects on humans. *Heliyon* **2020**, *6*, e04691. [CrossRef] [PubMed]
2. Jarvis, P.; Fawell, J. Lead in drinking water—An ongoing public health concern? *Curr. Opin. Environ. Sci. Health* **2021**, *20*, 100239. [CrossRef]
3. Clarkson, T.W.; Magos, L. The toxicology of mercury and its chemical compounds. *Crit. Rev. Toxicol.* **2006**, *36*, 609–662. [CrossRef]
4. Rinaudo, M. Chitin and chitosan: Properties and applications. *Prog. Polym. Sci.* **2006**, *31*, 603–632. [CrossRef]
5. Younes, I.; Rinaudo, M. Chitin and Chitosan Preparation from Marine Sources. Structure, Properties and Applications. *Mar. Drugs* **2015**, *13*, 1133–1174. [CrossRef]
6. Muzzarelli, R. Chitin and chitosan as chromatographic supports and adsorbents for collection of metal ions from organic and aqueous solutions and sea-water. *Talanta* **1969**, *16*, 1571–1577. [CrossRef]

7. Merrifield, J.D.; Davids, W.G.; MacRae, J.D.; Amirbahman, A. Uptake of mercury by thiol-grafted chitosan gel beads. *Water Res.* **2004**, *38*, 3132–3138. [CrossRef]
8. Delben, F.; Muzzarelli, R.A.A. Thermodynamic study of the interaction of N-Carboxymethyl chitosan with divalent metal ions. *Carbohydr. Polym.* **1989**, *11*, 221–232. [CrossRef]
9. Manzoor, K.; Ahmad, M.; Ahmad, S.; Ikram, S. Removal of Pd(ii) and Cd(ii) from wastewater using arginine cross-linked chitosan–carboxymethyl cellulose beads as green adsorbent. *RSC Adv.* **2019**, *9*, 7890–7902. [CrossRef]
10. Pearson, R.G. Hard and soft acids and bases. *J. Am. Chem. Soc.* **1963**, *85*, 3533–3539. [CrossRef]
11. Yan, X.; Rahman, S.; Rostami, M.; Tabasi, Z.A.; Khan, F.; Alodhayb, A.; Zhang, Y. Carbon Quantum Dot-Incorporated Chitosan Hydrogel for selective sensing of HG^{2+} ions: Synthesis, characterization, and density Functional Theory calculation. *ACS Omega* **2021**, *6*, 23504–23514. [CrossRef]
12. Jeremić, S.; Tran, T.H.; Marković, Z.; Ngo, T.C.; Dao, D.Q. Insight into interaction properties between mercury and lead cations with chitosan and chitin: Density functional theory studies. *Comput. Theor. Chem.* **2018**, *1138*, 99–106. [CrossRef]
13. Hassan, B.; Muraleedharan, K.; Mujeeb, V.M.A. Density functional theory studies of Pb (II) interaction with chitosan and its derivatives. *Int. J. Biol. Macromol.* **2015**, *74*, 483–488. [CrossRef]
14. Marenich, A.V.; Cramer, C.J.; Truhlar, D.G. Universal solvation model based on solute electron density and on a continuum model of the solvent defined by the bulk dielectric constant and atomic surface tensions. *J. Phys. Chem. B* **2009**, *113*, 6378–6396. [CrossRef] [PubMed]
15. Weinhold, F. Natural bond orbital analysis: A critical overview of relationships to alternative bonding perspectives. *J. Comput. Chem.* **2012**, *33*, 2363–2379. [CrossRef]
16. Bader, R.F.W. A quantum theory of molecular structure and its applications. *Chem. Rev.* **1991**, *91*, 893–928. [CrossRef]
17. Johnson, E.R.; Keinan, S.; Mori-Sánchez, P.; Contreras-García, J.; Cohen, A.J.; Yang, W. Revealing noncovalent interactions. *J. Am. Chem. Soc.* **2010**, *132*, 6498–6506. [CrossRef]
18. Lu, T.; Chen, F. Multiwfn: A multifunctional wavefunction analyzer. *J. Comput. Chem.* **2011**, *33*, 580–592. [CrossRef] [PubMed]
19. Terreux, R.; Domard, M.; Viton, C.; Domard, A. Interactions Study between the Copper II Ion and Constitutive Elements of Chitosan Structure by DFT Calculation. *Biomacromolecules* **2005**, *7*, 31–37. [CrossRef]
20. Vieira, R.S.; Beppu, M.M. Dynamic and static adsorption and desorption of Hg(II) ions on chitosan membranes and spheres. *Water Res.* **2006**, *40*, 1726–1734. [CrossRef] [PubMed]
21. Borsagli, F.G.L.M.; Mansur, A.A.P.; Chagas, P.; Oliveira, L.C.A.; Mansur, H.S. O-carboxymethyl functionalization of chitosan: Complexation and adsorption of Cd (II) and Cr (VI) as heavy metal pollutant ions. *React. Funct. Polym.* **2015**, *97*, 37–47. [CrossRef]
22. Mao, J.; Lin, S.; Lu, X.J.; Wu, X.H.; Zhou, T.; Yun, Y.-S. Ion-imprinted chitosan fiber for recovery of Pd(II): Obtaining high selectivity through selective adsorption and two-step desorption. *Environ. Res.* **2019**, *182*, 108995. [CrossRef]
23. Xu, Y.; Meng, X. Molecular simulation elaborating the mechanism of 1B-Hydroxy alantolactone inhibiting Ubiquitin-Conjugating enzyme UBCH5S. *Sci. Rep.* **2020**, *10*, 141. [CrossRef]
24. Lu, T. A comprehensive electron wavefunction analysis toolbox for chemists, Multiwfn. *J. Chem. Phys.* **2024**, *161*, 082503. [CrossRef]
25. Singh, R.; Smiatek, J.; Moerschbacher, B.M. Unraveling the Impact of Acetylation Patterns in Chitosan Oligomers on Cu^{2+} Ion Association: Insights from DFT Calculations. *Int. J. Mol. Sci.* **2023**, *24*, 13792. [CrossRef] [PubMed]
26. Aranaz, I.; Alcántara, A.R.; Civera, M.C.; Arias, C.; Elorza, B.; Heras Caballero, A.; Acosta, N. Chitosan: An overview of its properties and applications. *Polymers* **2021**, *13*, 3256. [CrossRef] [PubMed]
27. Wang, W.; Meng, Q.; Li, Q.; Liu, J.; Zhou, M.; Jin, Z.; Zhao, K. Chitosan derivatives and their application in biomedicine. *Int. J. Mol. Sci.* **2020**, *21*, 487. [CrossRef] [PubMed]
28. Dünnhaupt, S.; Barthelmes, J.; Thurner, C.C.; Waldner, C.; Sakloetsakun, D.; Bernkop-Schnürch, A. S-protected thiolated chitosan: Synthesis and in vitro characterization. *Carbohydr. Polym.* **2012**, *90*, 765–772. [CrossRef]
29. Luo, W.; Bai, Z.; Zhu, Y. Fast removal of Co(ii) from aqueous solution using porous carboxymethyl chitosan beads and its adsorption mechanism. *RSC Adv.* **2018**, *8*, 13370–13387. [CrossRef]
30. Muller, P. Glossary of terms used in physical organic chemistry (IUPAC Recommendations 1994). *Pure Appl. Chem.* **1994**, *66*, 1077–1184. [CrossRef]
31. Martell, A.E.; Hancock, R.D. *Metal Complexes in Aqueous Solutions*; Springer: Berlin/Heidelberg, Germany, 1996. [CrossRef]
32. Makov, G.; Payne, M.C. Periodic boundary conditions in ab initio calculations. *Phys. Rev. B Condens. Matter* **1995**, *51*, 4014–4022. [CrossRef]
33. Frisch, M.J.; Trucks, G.W.; Schlegel, H.B.; Scuseria, G.E.; Robb, M.A.; Cheeseman, J.R.; Scalmani, G. *Gaussian 16*; Gaussian, Inc.: Wallingford, CT, USA, 2016.
34. Zhao, Y.; Truhlar, D.G. The M06 suite of density functionals for main group thermochemistry, thermochemical kinetics, noncovalent interactions, excited states, and transition elements: Two new functionals and systematic testing of four M06-class functionals and 12 other functionals. *Theor. Chem. Acc.* **2007**, *120*, 215–241. [CrossRef]

35. Chai, J.-D.; Head-Gordon, M. Long-range corrected hybrid density functionals with damped atom–atom dispersion corrections. *Phys. Chem. Chem. Phys.* **2008**, *10*, 6615–6620. [CrossRef]
36. Grimme, S.; Antony, J.; Ehrlich, S.; Krieg, H. A consistent and accurate ab initio parameterization of density functional dispersion correction (DFT-D) for the 94 elements H-Pu. *J. Chem. Phys.* **2010**, *132*, 154104. [CrossRef] [PubMed]
37. Hay, P.J.; Wadt, W.R. Ab initio effective core potentials for molecular calculations. Potentials for the transition metal atoms Sc to Hg. *J. Chem. Phys.* **1985**, *82*, 270–283. [CrossRef]
38. Tomasi, J.; Mennucci, B.; Cammi, R. Quantum Mechanical continuum solvation models. *Chem. Rev.* **2005**, *105*, 2999–3094. [CrossRef] [PubMed]
39. Scalmani, G.; Frisch, M.J. Continuous surface charge polarizable continuum models of solvation. I. General formalism. *J. Chem. Phys.* **2010**, *132*, 114110. [CrossRef] [PubMed]
40. Pliego, J.R.; Riveros, J.M. The Cluster−Continuum model for the calculation of the solvation free energy of ionic species. *J. Phys. Chem. A* **2001**, *105*, 7241–7247. [CrossRef]
41. Fernández, J.A.H.; Carrascal, J.; Palomo, J.A.P. Comparative DFT study of lignocellulosic binder on N- and S-Monodoped graphene for sustainable Li-Ion battery electrodes. *J. Compos. Sci.* **2026**, *10*, 70. [CrossRef]
42. Palomo, J.A.P.; Zabala, J.E.H.; Fernández, J.A.H. DFT Study of PVA Biocomposite/Oyster Shell ($CaCO_3$) for the Removal of Heavy Metals from Wastewater. *J. Compos. Sci.* **2025**, *9*, 340. [CrossRef]
43. Fernández, J.H.; Palomo, J.P.; Ortega-Toro, R. Application of DFT and Experimental Tests for the Study of Compost Formation Between Chitosan-1,3-dichloroketone with Uses for the Removal of Heavy Metals in Wastewater. *J. Compos. Sci.* **2025**, *9*, 91. [CrossRef]

Disclaimer/Publisher's Note: The statements, opinions and data contained in all publications are solely those of the individual author(s) and contributor(s) and not of MDPI and/or the editor(s). MDPI and/or the editor(s) disclaim responsibility for any injury to people or property resulting from any ideas, methods, instructions or products referred to in the content.